Soft Matter

PAPER

View Article Online
View Journal | View Issue

Cite this: *Soft Matter*, 2020, **16**, 6572

3D aggregation of cells in packed microgel media†

Cameron D. Morley, *[a] Jesse Tordoff,[b] Christopher S. O'Bryan, [a] Ron Weiss[bcd] and Thomas E. Angelini [aef]

Received 24th March 2020,
Accepted 19th June 2020

DOI: 10.1039/d0sm00517g

rsc.li/soft-matter-journal

In both natural and applied contexts, investigating cell self-assembly and aggregation within controlled 3D environments leads to improved understanding of how structured cell assemblies emerge, what determines their shapes and sizes, and whether their structural features are stable. However, the inherent limits of using solid scaffolding or liquid spheroid culture for this purpose restrict experimental freedom in studies of cell self-assembly. Here we investigate multi-cellular self-assembly using a 3D culture medium made from packed microgels as a bridge between the extremes of solid scaffolds and liquid culture. We find that cells dispersed at different volume fractions in this microgel-based 3D culture media aggregate into clusters of different sizes and shapes, forming large system-spanning networks at the highest cell densities. We find that the transitions between different states of assembly can be controlled by the level of cell–cell cohesion and by the yield stress of the packed microgel environment. Measurements of aggregate fractal dimension show that those with increased cell–cell cohesion are less sphere-like and more irregularly shaped, indicating that cell stickiness inhibits rearrangements in aggregates, in analogy to the assembly of colloids with strong cohesive bonds. Thus, the effective surface tension often expected to emerge from increased cell cohesion is suppressed in this type of cell self-assembly.

1 Introduction

Across the disciplines of developmental biology, regenerative medicine, and tissue engineering, researchers seek to understand how structured cell assemblies emerge, what determines their shapes and sizes, and whether their structural features are stable.[1–7] Using controlled 3D environments to investigate cell self-assembly and aggregation is critical for developing understanding of the relationship between multicellular spatial structure and cell–cell interactions. In 3D culture, these controlled environments historically have been either solid scaffolds or liquid culture media. For example, the self-assembly of endothelial cells into capillary networks, known as vasculogenesis, is often performed in biopolymer scaffolds like Matrigel.[6,8–10] Stronger porous scaffolds are often implanted into the body in tissue engineering applications, sometimes seeded with cells before implantation.[11–13] These approaches help to uncover how extracellular matrix (ECM) scaffolding may influence cell assembly *in vivo* or how cells assemble within engineered scaffolding. By contrast, scaffold free self-assembly is often performed in liquids, where spheroids spontaneously assemble at the bottom of low adhesion wells.[14–17] Investigations of cell rearrangements, aggregation, and segregation of different cell types can be performed in these spheroids without the dominating influence of a solid scaffold.[15–17]

In several ways, these two opposing and general approaches to assembling cells reveal the advantages and disadvantages of one another. For example, complex multicellular shapes can emerge in solid scaffolds, yet the scaffold's elasticity or degradability can limit these processes and even trap single cells in place.[18–20] By contrast, spherical aggregates in liquid culture are unrestricted by solid surroundings and cells can freely rearrange within them, yet the details of spontaneous cell aggregation and self-assembly cannot be studied with this approach because cells are forced together by gravity and the walls of their container to form spheroids. Expanding beyond

[a] *Department of Mechanical and Aerospace Engineering, Herbert Wertheim College of Engineering, University of Florida, Gainesville, FL 32611, USA*
[b] *Department of Biological Engineering, Massachusetts Institute of Technology, Cambridge, MA, USA*
[c] *Massachusetts Institute of Technology, Koch Institute for Integrative Cancer Research, Cambridge, MA, USA*
[d] *Massachusetts Institute of Technology, Synthetic Biology Center, Cambridge, MA, USA*
[e] *Department of Materials Science and Engineering, Herbert Wertheim College of Engineering, University of Florida, Gainesville, FL 32611, USA*
[f] *J. Crayton Pruitt Family Department of Biomedical Engineering, Herbert Wertheim College of Engineering, University of Florida, Gainesville, FL 32611, USA*

† Electronic supplementary information (ESI) available: Microgel rheological characterization and evolution of cell volume fraction in time. See DOI: 10.1039/d0sm00517g

the extremes of liquids and solids as culture media, cell behavior has been studied in a diversity of more complex 3D environments, including entangled polymer networks, dynamic viscoelastic hydrogels, cohesive functionalized microgels, and density matched liquid media.[21–24] This work points toward the possibility of richer investigations of multicellular self-assembly, enabled by 3D culture materials that exhibit the advantageous features of both solid scaffolds and liquid spheroid culture. Such a 3D medium would have to exhibit solid-like properties to prevent dispersed cells from sinking under gravitational forces and potentially to prevent aggregates from balling up into spheroids. Simultaneously, this medium would exhibit features of spheroid culture in liquid, such as the ability to focus on the role of cell–cell interactions in self-assembly without the dominating role of a solid ECM network. While such an approach would not recapitulate the environments cells experience in tissues, it would enable a diversity of research questions to be posed and investigated that currently represent a gap in our capabilities and understanding of cell assembly and aggregation in 3D.

Here, we investigate the 3D self-assembly of cell aggregates in a non-adhesive, reconfigurable, three-dimensional cell culture environment made from packed hydrogel microparticles. At packing densities above a threshold value microgels exhibit solid-like responses to low levels of applied stress, and when stresses exceed their yield stress, σ_y, they re-arrange; when stresses are removed, they return to the solid-like state[25–33] (Fig. S1, ESI†). Leveraging this property, we disperse Chinese Hamster Ovary (CHO) cells in packed microgels swollen in liquid culture media. We find that cells dispersed in this microgel-based 3D culture media are able to aggregate and, depending on the volume fraction of cells seeded into the microgels, aggregates of different sizes and shapes emerge over the course of 48 h. At extremely low cell densities, no significant aggregation is observed; at intermediate cell densities, small dispersed aggregates form; at high cell densities, large system-spanning networks of cell aggregates form. By repeating experiments using cells expressing increased levels of E-cadherin, we find that the transitions between these types of aggregate occur at lower cell densities with increased levels of cell–cell cohesion. We also find that these transitions can be controlled by the yield stress of the packed microgel medium. By analyzing the fractal dimension of aggregates, we find those with increased cell–cell cohesion to be less sphere-like and more irregularly shaped, indicating that cell stickiness inhibits rearrangements in aggregates, in analogy to how colloids with strong cohesive bonds are known to aggregate. This result indicates the effective surface tension that is expected to emerge from increased cell cohesion is suppressed in this type of cell self-assembly.

2 Materials and methods

2.1 Microgel fabrication

Polyacrylamide (pAAM) microgel particles crosslinked with 2 mol% *N*,*N*′-methylenebisacrylamide (BIS) are prepared through a precipitation polymerization in ethanol. A solution containing 40 g of acrylamide monomer, 1.77 g of *N*,*N*′-methylenebisacrylamide, and 500 mg of azobisisobutyronitrile is prepared in 500 mL of ethanol in a 1 L round bottom flask. The solution is sparged with nitrogen for 30 minutes and then placed in a preheated oil bath at 60 °C for 4 h under continuous stirring. After approximately 30 min, a white precipitate begins to form, and the solution becomes hazy. Once the polymerization is completed, the precipitate is collected by vacuum filtration and rinsed with ethanol on the filter. Afterwards, the precipitate is dispersed in 1 L of ethanol under continuous stirring conditions for 18 h. The precipitate is again collected by vacuum filtration and dried on a filter for ~10 min. Finally, the microparticles are dried completely in a vacuum oven at 50 °C to yield a loose white powder. In order to determine the fully swollen microgel size, we dilute the loose powder to a concentration <0.1% in a glass bottom dish and image the dilute mixture using phase contrast microscopy (Fig. S2a, ESI†). In imageJ we measure the cross-sectional area of each microgel particle and equate each area to that of an equivalent circle. Calculating the equivalent particle diameter and generating a histogram, we find the average particle diameter is 5–6 μm (Fig. S2b, ESI†). Based on the composition off the microgels and our previous work, we expect that the individual gels have elastic moduli of order 10 kPa.[34]

2.2 Cell culture

Chinese hamster ovary cells (CHO), are cultured in Dulbecco's Modified Eagle Medium (DMEM) with 4.5 g L^{-1} glucose, L-glutamine, and sodium pyruvate supplemented with 10% FBS, 1% non-essential amino acids (NEAA) and 1% penicillin streptomycin. After cells reach 50–70% confluence, they are dyed with 5-chloromethylfluorescein diacetate (CMFDA) or calcein red-orange AM. A 10 mM working stock CMFDA solution is prepared in dimethyl sulfoxide (DMSO). At the time cells are dyed, the stock solution is further diluted to 10 μM concentration and added to the culture dish. Similarly, a stock calcein red-orange solution is diluted to a final concentration of 5 μM in the culture dish. After 30 min, the dye solution is removed, fresh media is added, and the dish is incubated for an additional 30 min. The dish is then washed with phosphate buffered saline (PBS), and incubated in 3 mL of 5% trypsin–EDTA solution for 5 min. The cells are harvested from the plate and placed into a 15 mL centrifuge tube and centrifuged to pellet the cells.

2.3 Microgel and dispersal preparation

Microgel particles are swollen in CHO liquid media to generate the jammed 3D support material for cell dispersal experiments, prepared at concentrations between 4% and 8% polymer (w/w). Our rheological tests confirm that within this concentration range the microgels are jammed, filling space with a porous and dominantly solid-like packing of soft spheres (Fig. S1, ESI†). They achieve jamming at this low polymer concentration range because they are swollen with cell-growth media. In this low concentration range, microgels likely deform and fill in pore space without significantly changing volume with increasing polymer concentration, as polyacrylamide has been shown to

resist compression when applied pressure is below the osmotic pressure of the polymer network.[34,35]

To prepare the gels for cell seeding, 1.5 mL of microgel media is loaded into a glass-bottomed well and incubated at 37 °C and 5% CO_2 for one hour. We control cell seeding density by weighing the wet cell pellet in its centrifuge tube and mixing with the appropriate amount of microgel media, empirically tuning this procedure to achieve reproducible seeding. Before depositing cells into the microgel media, the pellet is gently dispersed with a micropipette. The dispersed cells are then deposited into the microgel media, and gently pipette mixed to achieve uniform cell distribution. While this method is useful in achieving an approximate seeding density within the gel, the cell volume fraction is determined and reported based on the image analysis (Section 2.5).

2.4 Ecad+ cell line generation

The cell line expressing E-cadherin was constructed using the CHO K1 landing pad cell line, as described in previous works.[36] In short, the integration vector consisted of two transcriptional units: phEF1a (human elongation factor promotor) driving expression of a mouse E-cadherin coding sequence, and phEF1a driving expression of mKate fluorescent protein coding sequence. The payload vector was constructed with LR clonase-based assembly. 300 ng of the integration vector was co-transfected with 300 ng of CAG-Bxb1 using Viafect into the landing pad cell lines. Media with 8 μg mL^{-1} puromycin was added three days after transfection, and cells were collected and used after at least two weeks of selection and recovery. We confirmed E-cadherin expression in the CHO cell lines by staining with an anti-mouse/human E-cadherin antibody. Integration of sequences was verified through FACS analysis, in which the Ecad+ CHO cells exhibited a strong signal that was absent in wild type CHO cells. Cells were maintained in Dulbecco's modified Eagles medium (DMEM) media supplemented with 10% FBS and 1% non-essential amino acids (NEAA). Media was changed and cells were passaged as needed.

2.5 Image collection and processing

To monitor aggregate formation, we collect 3D stacks of fluorescence images using a Nikon laser scanning confocal microscope with a C2+ scan head and 20× objective with a numerical aperture (NA) of 0.75. The laser is scanned using a pixel dwell time of 4.8 μs and at a power setting such that photobleaching does not occur over the duration of the experiments. The 0.75 NA objective has a lateral optical resolution of 325 nm with green illumination and 374 nm with red illumination; the axial resolution is 0.889 μm for green light and 1.022 μm for red light. We collect images with a spatial sampling frequency of 1.244 μm per px in the *X*–*Y* plane and 1.5 μm per step in the *Z* direction. Considering these optical resolution limits and spatial sampling frequencies, we expect blurring from the 3D point spread function along all directions to be small relative to the size of the aggregates and even single cells, which have characteristic length-scales of more than 10× the spatial sampling frequency. Quantitative analysis of the cross-sectional areas of cells and clusters measured along different directions revealed no major differences, so we chose not to deconvolve the point-spread-function from the *z*-stacks. To remove random noise, the images are blurred with a Gaussian kernel having a half-width of 0.7 pixels. Since the sampling frequency along the *z*-axis is different from that in the *x*–*y* plane, we interpolate the stacks and re-sample along the *z*-axis, creating cubic voxels. The step-size of the focal point relative to the objective turret is accounted for in this process. We then take the logarithm of the intensity distribution to reduce the cell-to-cell variability in fluorescence intensity. These processed images are then segmented using Otsu's thresholding method. Cell volume fraction, ϕ, is determined from the ratio of segmented voxel number to the total number of voxels. Spatially connected regions in the segmented stack are labeled using the bwlabeln function in MATLAB, and individual clusters were analyzed using the regionprops and regionprops3 functions.

3 Results and discussion

To investigate cell aggregation in packed microgels, we seed CHO cells in the 3D microgel media at different volume fractions, ϕ_0, and monitor their progression in time using confocal fluorescence microscopy. Exploring cell aggregation in a non-adhesive environment like pAAm microgels may require a cell type whose viability is not dependent on anchorage to an extracellular matrix. CHO cells are good candidates for this approach since they can be cultured in suspension.[37,38] In this respect, using microgels as a 3D culture medium is like having a solid analog of liquid culture. We note that in traditional 3D suspension culture there is generally a time-dependent proliferation rate coupled to cell density.[37,38] Typically, cells in liquid culture do not proliferate significantly for approximately two days after seeding. We find a similar lag in proliferation for cells dispersed in microgels and we leverage this behavior in our experiments (Fig. S3, ESI†). Here we report data collected during the first two days after seeding (Fig. 1).

3.1 Merging of cells and clusters into networks

To observe how aggregation occurs, we collect *z*-stacks of fluorescence images every 12 h and also perform faster time-lapses, collecting stacks every 20 minutes. Within each 12 h snapshot of samples prepared at different ϕ_0, we see denser distributions of cells and increased occurrences of multi-cellular structures with increasing ϕ_0. At low ϕ_0, we see very little time-dependence by visual examination, indicating the cells do not migrate to one another to form aggregates. By contrast, at intermediate and large ϕ_0, we see coarsening occurring in the system; initially dispersed cells appear to merge into clusters or extremely large network-like aggregates (Fig. 1b). These general behaviors are found for the wild type (WT) cells and the cells expressing higher levels of E-cadherin (Ecad+). To quantitatively analyze the relationship between volume fraction and aggregate size and shape, the fluorescence images are thresholded; the qualitative progression of aggregate formation can be seen even more clearly in these thresholded images (Fig. 1c and d).

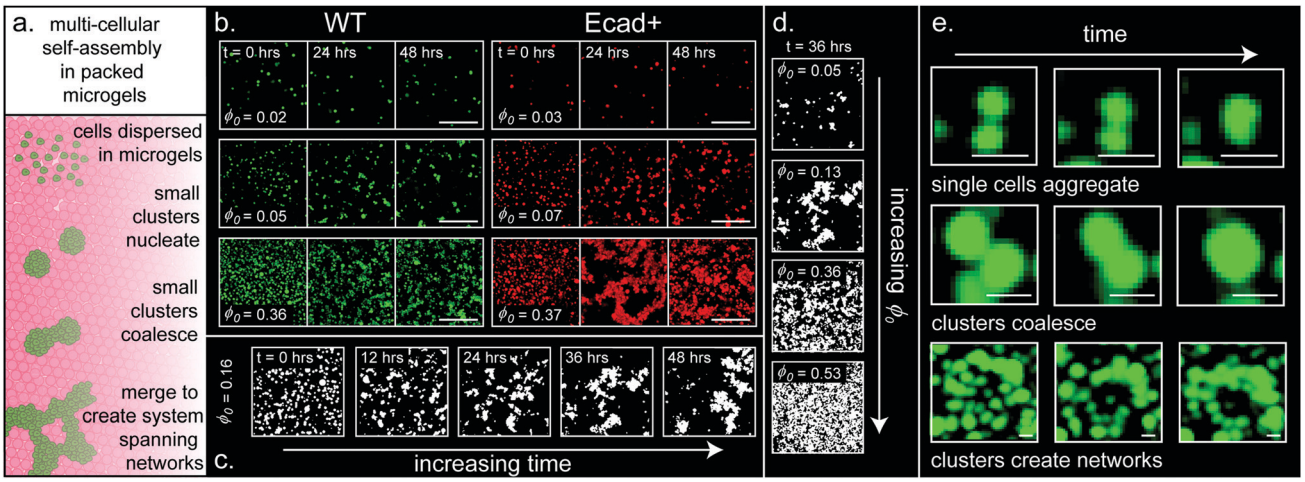

Fig. 1 3D aggregation in packed microgels. (a) A 3D microgel culture environment allows single cells to aggregate and aggregates to coalesce without significant build-up of mechanical stress and without the need for a degradable scaffolding. (b) We disperse CHO cells having different cohesive strength (WT and Ecad+) into packed microgels, seeding at various volume fractions, ϕ_0. We collect 3D fluorescence data using confocal microscopy. Single slices through the z-stacks show that single cells remain dispersed at low ϕ_0 and generate small aggregates at intermediate ϕ_0. Samples at large ϕ_0 exhibit irregularly shaped assemblies having network-like structure (scale bars = 250 μm). (c) For a sample prepared at intermediate ϕ_0, thresholded images show single cells and small clusters merging to form fewer, larger aggregates. (d) Thresholded images of samples prepared at different ϕ_0 and measured at the same time-point show how assembly depends on seeding density. (e) Single cells merge to form small aggregates, small aggregates coalesce to form larger aggregates, and large aggregates link to form networks (scale bars = 25 μm).

To directly observe how these different assemblies emerge at shorter time intervals, we examine the images taken every 20 minutes (Movie S1, ESI†). In this time-lapse video, we find single cells aggregating, multi-cellular clusters merging, and elongated and irregularly shaped clusters forming from smaller clusters (Fig. 1e and Movies S1–S4, ESI†). We rarely see cell divisions over 48 h, and similarly we do not see major changes in total volume fraction (Fig. S3, ESI†). However, we cannot rule out that division occurs in samples seeded at very high densities or within large aggregates; the experiments performed here are not suited to identify cell division events in dense aggregates. We also do not observe translocation of cells beyond distances of about 1 cell diameter. Cells within this distance of one another appear able to spontaneously interconnect, yet cells far from one another at low volume fractions remain isolated and stationary. This lack of migration is expected for CHO cells that require adhesions for motility, in contrast to T cells which can migrate through microgels, likely using their amoeboid-like migration mechanisms.[29,39] To measure how these stationary single cells and multicellular aggregates explore the space around them, we track isolated objects in time and measure the mean-square-fluctuations in their longest dimension, $L(t)$, as a function of delay time, τ, given by $\Delta L^2(\tau) = \langle (L(t+\tau) - L(t))^2 \rangle_t$, where the angle brackets indicate an average over time τ. We find that $\Delta L^2(\tau)$ exhibits no clear dependence on aggregate size, enabling an ensemble average to be taken at each delay time, τ (see Supplemental Text and Fig. S4, ESI†). We find that at delay times of about 6 h, the average fluctuation of $L(t)$ is about 11 μm in size, or about one cell radius. In later sections we discuss how this fluctuation in cell extent may play a key role in setting the threshold volume fraction for aggregation to occur.

3.2 Emergence of the largest aggregate

To quantitatively study how single cells merge into system-spanning aggregates, we analyze the thresholded fluorescence images of cells in the 3D microgel medium (Fig. 1c and d). Given the limitations of imaging deep into the sample along the optical axis (Z-axis), and the large 1270 μm by 1270 μm field of view in the X–Y plane, achieved by stitching multiple adjacent z-stacks together, we choose to measure the cross-sectional area of all separate aggregates identified in each imaging plane. The lowest imaging plane is chosen to be approximately 100 μm away from the sample dish to avoid wall-effects and ensure that the system is isotropic. We analyze the slices in each volume to identify the largest aggregate and measure its area, A_L. We normalized A_L by the measured system area, A_m, and examine how the ratio evolves over time, t, and how it varies with the instantaneous volume fraction of cells in the sample, ϕ (Fig. 2). We normalize A_L by A_m rather than reporting the area values because this normalized parameter can be used to identify universal behaviors found in all percolating systems. To check the quality of our imaging as a function of depth into the sample, we also analyze A_L/A_m in each plane, finding no dominating or systematic increase or decrease (Fig. S5, ESI†). We also note that the upper bound on measurement uncertainty of A_L is less than the area of a one-cell-thick perimeter; there is negligible uncertainty in A_m since it is the field of view area. Thus, errorbars in nearly all the A_L/A_m measurements displayed in Fig. 2 are comparable to or less than the sizes of the symbols plotted. We find that at the lowest seeding densities and highest seeding density, A_L/A_m is independent of time while at intermediate seeding densities, the largest aggregate size increases over time (Fig. 2a). At these intermediate seeding densities, we see that the largest

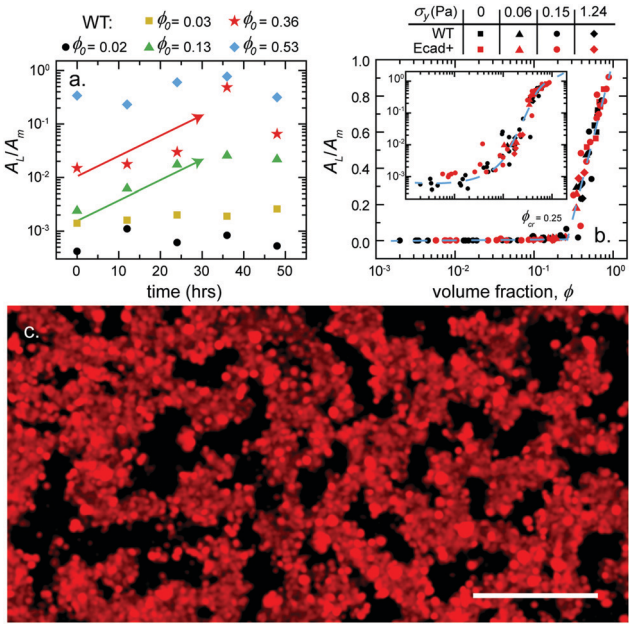

Fig. 2 To determine a measure of the proportion of space occupied by the largest self-assembled structure within each sample and at each time-point, the cross-sectional area of the largest aggregate, A_L, is measured and divided by the entire measured area, A_m. (a) The largest aggregates in samples prepared at low and high ϕ_0 exhibit little evolution in time, while the largest aggregates in samples prepared at intermediate ϕ_0 exhibit very strong growth. These data were collected from five individual samples prepared in microgel medium having a yield stress of 0.15 Pa. (b) The largest aggregate sizes in samples prepared from different cell types and using microgel media having different yield stresses appear to lay on a universal curve when plotted against each sample's volume fraction, ϕ. Examining the data on a semilog-x scale, there appears to be a crossover volume fraction, ϕ_{cr}, of about 0.25, above which the size of the largest aggregate is strongly dependent on cell packing density. The same data appear to follow a sigmoid-shaped curve when plotted on a log–log scale, where ϕ_{cr} lays about halfway up the curve. (c) A sample prepared at ϕ_0 = 0.37 imaged at t = 36 h exhibits a system spanning network. Scale bar = 250 μm.

aggregates grow up to 10× their original size. At the latest times, we see that the largest aggregate size appears to marginally decrease. This stage may reflect the slow evolution of large aggregates after all the smaller clusters have merged.

The time-dependence and cell density dependence of A_L/A_m shown in Fig. 2a corresponds to WT cells in microgel medium having a yield stress of σ_y = 0.15 Pa. Samples prepared in microgel media having different σ_y levels, and samples prepared using the Ecad+ cells, all show this general trend. We also tested microgel media having particle packing fractions slightly below the jamming threshold, where σ_y = 0 Pa. While this system is technically a liquid, the same general trend was also observed, indicating that the cells are still supported by the looser microgel packs. Inspired by systems exhibiting percolation transitions, we tested whether the growth of the largest aggregate can be collapsed onto a universal curve controlled by the average fraction of space occupied by cells. Thus, we re-plot all these data together *versus* their corresponding volume fractions, ϕ, finding a reasonable data collapse onto a single curve. Plotted on a semilog-x scale, the transition from stationary cells to growing aggregates appears to occur at $\phi \approx 0.25$. On a log–log scale, the same data follows a sigmoidal trend and the $\phi \approx 0.25$ occurs about half-way up the curve (Fig. 2b). These combined data illustrate how 8 different experimental conditions spanning 3 decades in volume fraction collapse onto a single curve, albeit with some spread in the data. While no one condition is shown in replicate, the potential differences in the transition point across the different samples are small compared to the noise in the data, showing how the cell density itself exhibits a strong influence on the point at which large aggregates begin to emerge for all samples. At high volume fractions, these large aggregates have the appearance of system-spanning percolated networks (Fig. 2c), which we analyze further in later sections. In traditional 3D percolating systems, the transition tends to occur at volume fractions between 0.16 and 0.29, depending on the particle aspect ratio.[40–43] The percolation threshold for perfect spheres is closer to the high end of this range[40,41] while transitions for ellipsoids lay at the lower end of the range.[41–43] In the case of cell percolation, the threshold may arise from average cell shape or the apparent ability of cells to reach out to one another over a modest distance, comparable to the cell size.

3.3 Identifying structures by volume-specific volume fraction

Since there is only one largest aggregate appearing in each sample and larger aggregates become less abundant as aggregation proceeds, we re-analyze the fluorescence data by measuring the volume fractions of sub-groups of clusters having a volume, V, falling within volume-bins. This procedure identifies the groups of clusters of approximately the same size that, together, occupy the most space in the sample. As we began to compute this volume-specific volume fraction, $\tilde{\phi}(V)$, we found that the distributions were log-normal, so we created volume bins logarithmically spaced at 5 bins per decade (Fig. 3a). Plots of $\tilde{\phi}(V)$ *versus* bin volume, V, exhibit peaks corresponding to the volumes of clusters occupying the most space in the sample, V_{cl}. Normalizing V_{cl} by the total measurement volume, V_m, we determine the volume fraction occupied by clusters of the representative size, which we believe is a more intuitive measure of cluster size than raw volume (Fig. 3b). Plots of V_{cl}/V_m *versus* volume fraction, ϕ, reveal information about cell aggregation that was not seen when analyzing only the largest aggregates. For example, a transition in aggregation behavior is seen at approximately 4% volume fraction, and a second transition occurs near 25% volume fraction. This second transition exhibits a large discontinuous jump in V_{cl}/V_m with increasing ϕ, while the first transition emerges smoothly from the plateau at small volume fractions. Quantitative size and shape analysis in Section 3.5 show that below 4% volume fraction, the samples dominantly contain single cells, while multicellular clusters form between 4% and 25% volume fraction, and system spanning structures emerge above 25% cell volume fraction. Visually inspecting the images verifies that the transition at 4% volume fraction corresponds to when single cells begin to merge into small, discrete clusters. This early transition was not

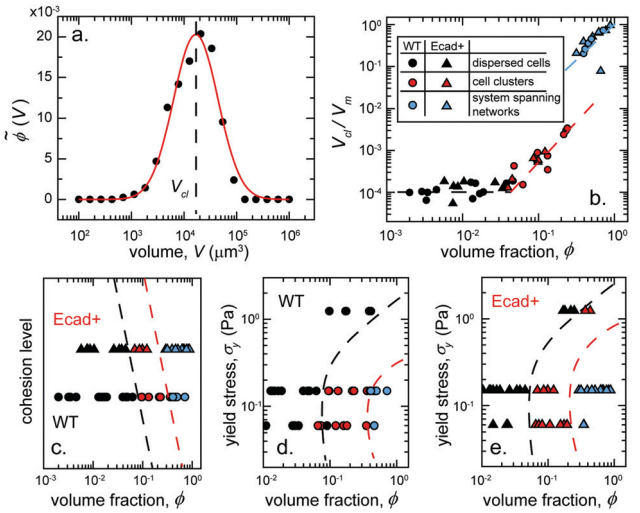

Fig. 3 Classifying assemblies and identifying transition boundaries. (a) We identify the clusters of approximately the same size and compute a volume-specific volume fraction, $\tilde{\phi}(V)$. We find that $\tilde{\phi}(V)$ has a log-normal shape and by identifying its peak location, we determine the characteristic volume of clusters occupying the most space in the sample, V_{cl}. (b) The volume fraction of these dominating clusters is determined by dividing V_{cl} by the measured system volume, V_m. Plotting V_{cl}/V_m *versus* volume fraction, ϕ, we find different types of assembles exhibit qualitatively different trends. Small clusters emerge smoothly from single cells with increasing ϕ, while networks emerge discontinuously from the smaller clusters. (c) Qualitatively labelling Ecad+ cells as "high" cohesion and WT cells as "low" cohesion, we see the transitions between different states of assembly occur at lower volume fractions for the high cohesion cells. These data correspond to samples prepared in packed microgels having a yield stress of 0.15 Pa. (d) WT cells in high yield stress (1.25 Pa) microgels are unable to cluster, while Ecad+ cells in the same microgels can cluster (e). For both cell types, at lower yield stresses (0.05 Pa), the microgels have diminished effects on the boundaries between the different types of cell assembly.

observed in the previous analysis of only the largest aggregates (Fig. 2). Direct inspection of the images also verifies that the transition at 25% volume fraction corresponds to when discrete clusters merge into system-spanning networks; this transition appears to have been captured by the previous analysis of the largest aggregates. The data plotted in Fig. 3b correspond to two samples containing WT and Ecad+, both employing microgel medium having a yield stress of $\sigma_y = 0.15$ Pa. In Section 3.4 we explore the roles of adhesion and yield stress in determining these transition points.

To investigate what physical factors may set the threshold volume fraction of 0.04 for the first transition we see here, we estimate the cell–cell spacing and compare it to the fluctuations in cell extent described in Section 3.1 and in the ESI.† Approximating the volume fraction of cells as $\phi \simeq v_{cell}/R_{cc}^3$, where v_{cell} is the volume of a single cell and R_{cc} is the center-to-center distance between cells, we can estimate the surface-to-surface distance of the cells at a given volume fraction, ϕ. Aggregate formation first occurs at $\phi \simeq 0.04$, where $v_{cell} \simeq 4500$ μm^3 (10 μm equivalent radius), corresponding to $R_{cc} \simeq 48$ μm. Subtracting one cell diameter gives a surface-to-surface distance of 28 μm; if every pair of cells has to reach across this divide to touch, they would have to extend by 14 μm. Considering that we find cells fluctuate in extent by about 11 μm, as described above, we believe these fluctuations set the threshold observed here.

3.4 Cohesion and yield stress shift aggregation transitions

While the data in Fig. 3b appear to lay on one curve, analyzing them separately reveals how the boundaries in these different states of aggregation depend on cell–cell cohesion. Without a quantitative measure of the cohesive energy density between the different cell types, we generally consider the Ecad+ cells to have "high" cohesion levels and WT cells to have "low" cohesion levels, and we plot the different types assembly *versus* ϕ (Fig. 3c). We find that the WT cells transition between different states of assembly at 2 to 3 times the volume fractions relative to where the Ecad+ cells exhibit the same transitions (Fig. 3c–e). While it is natural to expect more cohesive objects to require less packing in order to merge into clusters or networks, we were surprised by this result because both transitions involve discrete objects merging into one another from a finite separation distance. This difference may arise from non-specific adhesion of E-cadherin to the microgels, enabling some form of localized motility to occur, or it is possible that the Ecad+ cells exhibit more internally driven dynamics, creating surface fluctuations that overcome the barriers created by the packed microgels.

To investigate how the barriers created by packed microgels influence cell aggregation, we perform the same aggregate volume analysis described above on samples prepared in microgel media having different levels of yield stress, σ_y. In the most packed microgel systems with the highest yield stress, $\sigma_y = 1.5$ Pa and 8% polymer, the WT cells are unable to aggregate; they remain single cell dispersions at cell volume fractions up to $\phi = 0.4$. By contrast, the Ecad+ cells in the same packed microgels can form clusters at cell volume fractions of approximately $\phi = 0.3$ with a transition occurring at approximately $\phi = 0.25$. Reducing the yield stress to $\sigma_y = 0.15$ Pa at 5% polymer and lowering the barrier created by the microgels returns the transition values back to those described above for WT and Ecad+ cells with no further apparent dependence on yield stress as it is lowered further to $\sigma_y = 0.05$ Pa at 4% polymer (Fig. 3d and e). We expect that these measurements of the stress levels required for cells and cell clusters to merge and form the different structures seen here can be used in models of cell aggregation to quantify their cohesive energy densities.

3.5 Analyzing cluster and network shapes

To quantify the shapes of clusters and networks, we compute a radius of gyration for each isolated object identified within every slice of the fluorescence z-stacks, given by

$$R_g = \sqrt{\frac{1}{N}\sum_{k=1}^{N}(\boldsymbol{r}_k - \boldsymbol{r}_c)^2},$$

where N is the number of pixels constituting the object, $\boldsymbol{r}_k$ is the position vector of the kth pixel, and $\boldsymbol{r}_c$ is the centroid of the object. Here we analyze 2D planar slices instead of volumes to enable characterization of large system-spanning structures

with many R_g measurements; the same considerations of sample isotropy described above enable this approach. As aggregates become very large, their volumes exceed the imaging volume we can access with our microscope, limited along the optical axis by the finite working distance of our objectives and by light attenuation into large densely packed structures. While all our measurements are affected by the finite imaging volume, much larger objects can be characterized by analyzing areas in 2D planes than by analyzing volumes in 3D stacks, as imaging along the optical axis is limited to fairly modest length-scales. By plotting each measurement of R_g *versus* the measured area of each object, A, we analyze the average fractal dimension, d_f, at each state of assembly using the relationship $R_g \sim A^{1/d_f}$. Since fractal dimension can be measured by analyzing entire volumes or examining slices through 3D objects, our choice to do analysis in 2D provides relatively more information by allowing objects to be sampled over larger length-scales without any relative disadvantages. Here, cross-sections of perfectly spherical objects will appear circular and exhibit $d_f = 2$; irregularly shaped objects with a larger surface-area to volume ratio will exhibit $d_f < 2$. We find that the $d_f = 2$ curve creates a lower limit for data-points on these plots, as expected (Fig. 4a). In all samples, the smaller objects like single cells and small clusters produce datapoints clustered very near $R_{g\,circ} = \sqrt{A/(2\pi)}$ as expected for cross-sections through spherical shapes. By contrast, larger objects deviate from this curve and exhibit a crossover value of area, A_c, above which no objects lay on the $R_{g\,circ}$ curve. All the measurements used in this analysis correspond to objects much larger than our spatial sampling frequency of 1.2–1.5 μm per px, so we do not expect a major influence of voxel-shape on d_f measurements. To investigate this deviation further, we compute the relative difference between $R_{g\,circ}$ and all data points, given by $\delta R_g = (R_{g\,circ} - R_g)/R_{g\,circ}$, which clearly shows the crossover point (Fig. 4b). We also find this deviation by grouping the R_g *versus* A data in bins logarithmically spaced at 25 bins per decade and computing average values in each bin. We determine fractal dimensions of small structures and large structures separately by fitting power laws to the binned datapoints in each regime, separately (Fig. 4c). To reduce clutter only half these binned data points are shown in Fig. 3c. Below we analyse the crossover cluster area, A_c, and the average cluster fractal dimension, d_f, *versus* volume fraction ϕ to gain insight into what determines the size-dependent shapes of cell assemblies.

3.6 Increased cohesion locks in shape fluctuations

To isolate the effects of cell–cell cohesion on aggregate shape, we analyze plots of A_c and d_f *versus* ϕ for samples having a yield stress of $\sigma_y = 0.15$ Pa, which exhibit both transitions shown in Fig. 3d and e. Here we maintain the different classifications of assemblies described in Section 3.3. We also note that these fractal dimensions came from unconstrained fits to data points, so noise in the datapoints and related errors in the measurements can lead to determining a fractal dimension greater than 2. Thus, while the true fractal dimension cannot be greater than 2, random errors can cause measurements of fractal dimension to be greater than 2.

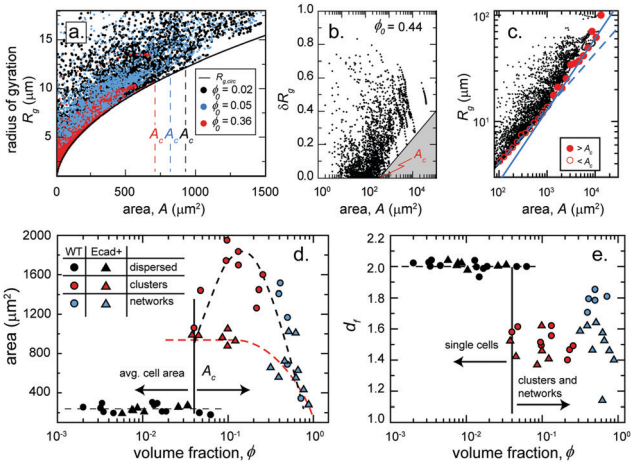

Fig. 4 Determining aggregate shapes in packed microgels (σ_y = 0.15 Pa). (a) Plotting the radius of gyration, R_g, *versus* cross-sectional area, A, for each measured aggregate, we find a diversity of aggregate shapes. The datapoints from the most compact aggregates lay close to the solid line, which corresponds to the theoretical curve for a perfect sphere. Many datasets exhibit a crossover aggregate area, A_c, above which no aggregates lay on the perfect sphere curve. (b) The deviation from perfect spherical shape is made clear by plotting the relative difference between the data points and the theoretical curve, δR_g, where it can be directly seen that no data points lay in the shaded region. (c) Averaging the R_g and A data-points in logarithmically spaced bins shows that aggregates smaller than A_c are more spherical (dashed blue line) and larger aggregates are more fractal (solid blue line). (d) At low cell densities, captured here by volume fraction, ϕ, no aggregates form and the average area of structures found corresponds to the single-cell cross-sectional area. At intermediate ϕ, small clusters form and A_c is generally lower for Ecad+ cells than for WT cells. At the highest cell densities, A_c begins to drop for both WT and Ecad+ cells as larger clusters join networks and smaller clusters remain isolated. (e) Single cells are nearly spherical, exhibiting $d_f \approx 2$. At intermediate ϕ, small clusters of WT and Ecad+ exhibit the same range of d_f, between 1.4 and 1.7. At the highest ϕ, WT cells exhibit higher d_f than Ecad+ cells, indicating that shape irregularities are locked in by cell–cell cohesion.

At the lowest volume fractions we find that there is no crossover area, A_c, where all objects appear to be single cells (Fig. 4d). Correspondingly, the average fractal dimension of the system is approximately 2 at these low cell densities (Fig. 4e). At intermediate volume fractions between $\phi \approx 0.04$ and 0.35, the system contains larger aggregates that deviate from the spherical shape having fractal dimensions between 1.4 and 1.7 (Fig. 4d and e). Within this window, we find that aggregates of low-cohesion WT cells generally exhibit larger A_c than the Ecad+ cells (Fig. 4d). Thus, at the same volume fraction, low-cohesion cells are able to form larger spherical aggregates than high-cohesion cells. The opposite trend would occur if cell cohesion created an effective interfacial tension that smooths out aggregate shape. We interpret this result to indicate that the re-arrangements of the stickier Ecad+ cells are inhibited relative to the low-cohesion WT cells during assembly, as would occur in sticky colloidal systems that have a lower relative cost of creating free surfaces. At the highest cell densities where networks begin to emerge, A_c begins to decrease with increasing volume fraction for both WT and Ecad+ assemblies (Fig. 4d). We interpret this result as a general consequence of larger clusters joining

networks with a higher probability than smaller clusters at a given cell density. Consistent with the cohesion-limited smoothing of structures, the stickier Ecad+ structures exhibit a lower fractal dimension than their WT counterparts, indicating that increased cohesion leads to the corresponding networks to have rougher surfaces (Fig. 4e). Detailed measurements of surface morphology and related fractal analysis is needed to test this interpretation. Taken together, these results and the transition behaviors found in the previous sections indicate that within a solid-like micro-environment without a specific cell adhesion capacity, cell–cell cohesion promotes aggregation while inhibiting the rearrangements required to smooth-out surface fluctuations.

4 Conclusions

Here we have investigated how cells assemble in packed microgels. This microgel medium represents a phase of soft matter that has been almost entirely unexplored as a 3D culture environment.[25–29] Packed microgels provide a dominantly solid-like environment having minimal adhesive interactions with the cells it supports, allowing aggregation and morphological change to occur without the significant build-up of elastic stress or the degradation of a biopolymer scaffolding. In this way, packed microgels perform like a solid analog to liquid culture in which cell assembly has been studied for decades.[15–17] However, in contrast to liquid suspension culture, we have found that in the microgel medium, cells can assemble into different kinds of structures determined by a balance between the properties of their surroundings and their cohesive interactions with one another. The transitions between the types of assemblies that emerge and the sizes of the assemblies depend on the cell volume fraction, the physical properties of the jammed microgel medium, and the level of cohesion between the cells. Preliminary tests indicate that fluctuations in the extent of single cells drive aggregation; these fluctuations do not strongly depend on the size of the objects, whether they are single cells or aggregates, and the overall amplitude of these fluctuations are about one cell diameter. Thus, aggregation appears to be driven by a single-cell fluctuation mechanism; isolated cells near one another or individual cells attached to the surfaces of assemblies fluctuate in shape and cohere when they encounter other cells.

Our findings share some aspects of cell aggregation recently found in 2D culture, in which multi-cellular structures emerge in a process called "motility limited aggregation," or MLA.[44] In MLA, the growth and fractal dimension of cell aggregates was found to depend on the rate of cell motility.[44] In contrast to the cells exhibiting MLA on 2D culture surfaces, the CHO cells studied here do not appear able to translocate using the known modes of cell motility that depend on integrin-mediated anchoring. We therefore believe that extending our investigation to many other cell types will reveal the same general behavior we find with CHO cells. Thus, interpreting aggregation in microgels based on underlying biomolecular and physicochemical dynamics of the cell requires further study. Specifically, our results point out the need to study how cell shape fluctuations or potential chemical signaling might mediate interactions between neighbors to facilitate connections between neighboring single cells or cell aggregates. Indeed, proximity-dependent cell dynamics was found previously with MCF10A cells dispersed in microgels.[26] These cells exhibited increasing extensional fluctuations along their long axis with increasing cell density. At the highest densities when cells were less than approximately one cell diameter from one another, their extensional fluctuations reduced. The thresholds found here may be found to depend on the same cell behaviors and further study of single cell shape fluctuations in microgels will further elucidate how cells aggregate in jammed microgel media.

We have not yet established physiological contexts for which packed microgel media is a good model; here we use the medium as a tool to study how cells aggregate in a controlled environment with minimal adhesion and anchorage. However, in recent 3D bioprinting work, structures made from multiple different cell types and ECM were supported by packed microgels, creating local micro-environments that better mimic *in vivo* contexts than microgels alone.[25,45] Similarly, microgels are increasingly used for 3D bioprinting in regenerative medicine and tissue engineering applications.[45–50] In one recent study, crosslinkable PEG microgels were utilized to stabilize 3D printed structures made from cells.[51] These microgels were also functionalized with RGD peptides that provide integrin binding sites to promote cell migration, proliferation, and ultimately a stable 3D tissue. In another recent study, microgels were used to template adhesive Fibrin networks by mixing fibrinogen and thrombin with microgels during polymerization, creating a porous matrix that cells could invade.[52] It would be interesting to investigate how cells aggregate in such adhesive microgel-based materials compared to those studied here, or to functionalize the microgels used here with RGD peptide to investigate the competing role of adhesion in cell aggregation in jammed microgels. Moving forward, we expect to see continuing growth in the use of microgels as a highly controllable 3D culture medium for fundamental study of multicellular behaviors, while at the same time we envision that 3D bioprinting applications leveraging packed microgels will continue to grow in number and diversity. We hope the study of cell aggregation in microgels described here will help to guide this future work.

Conflicts of interest

There are no conflicts to declare.

Acknowledgements

The authors thank Anton Paar for the use of the Anton Paar 702 rheometer through their VIP academic research program. This material is based on work supported by the National Science Foundation under grant no. DMR-1352043.

Notes and references

1 T. Mammoto and E. I. Donald, Mechanical control of tissue and organ development, *Development*, 2010, **137**(9), 1407–1420.

2 F. Pilot and T. Lecuit, Compartmentalized morphogenesis in epithelia: from cell to tissue shape, *Dev. Dyn.*, 2005, **232**(3), 685–694.
3 W. P. Daley, B. P. Sarah and M. Larsen, Extracellular matrix dynamics in development and regenerative medicine, *J. Cell Sci.*, 2008, **121**(3), 255–264.
4 D. M. Dean, *et al.*, Rods, tori, and honeycombs: the directed self-assembly of microtissues with prescribed microscale geometries, *FASEB J.*, 2007, **21**(14), 4005–4012.
5 N. Koike, *et al.*, Creation of long-lasting blood vessels, *Nature*, 2004, **428**(6979), 138–139.
6 J. M. Melero-Martin, *et al.*, Engineering robust and functional vascular networks *in vivo* with human adult and cord blood-derived progenitor cells, *Circ. Res.*, 2008, **103**(2), 194–202.
7 C.-P. Heisenberg and Y. Bellaïche, Forces in tissue morphogenesis and patterning, *Cell*, 2013, **153**(5), 948–962.
8 J. A. Rophael, *et al.*, Angiogenic growth factor synergism in a murine tissue engineering model of angiogenesis and adipogenesis, *Am. J. Pathol.*, 2007, **171**(6), 2048–2057.
9 C. P. Khoo, K. Micklem and S. M. Watt, A comparison of methods for quantifying angiogenesis in the Matrigel assay *in vitro*, *Tissue Eng., Part C*, 2011, **17**(9), 895–906.
10 Y. Kubota, *et al.*, Role of laminin and basement membrane in the morphological differentiation of human endothelial cells into capillary-like structures, *J. Cell Biol.*, 1988, **107**(4), 1589–1598.
11 S. J. Hollister, Porous scaffold design for tissue engineering, *Nat. Mater.*, 2005, **4**(7), 518–524.
12 F. J. O'brien, Biomaterials & scaffolds for tissue engineering, *Mater. Today*, 2011, **14**(3), 88–95.
13 J. L. Drury and J. M. David, Hydrogels for tissue engineering: scaffold design variables and applications, *Biomaterials*, 2003, **24**(24), 4337–4351.
14 E. Fennema, *et al.*, Spheroid culture as a tool for creating 3D complex tissues, *Trends Biotechnol.*, 2013, **31**(2), 108–115.
15 R. A. Foty and S. S. Malcolm, Cadherin-mediated cell-cell adhesion and tissue segregation in relation to malignancy, *Int. J. Dev. Biol.*, 2004, **48**(5-6), 397–409.
16 R. A. Foty and S. S. Malcolm, The differential adhesion hypothesis: a direct evaluation, *Dev. Biol.*, 2005, **278**(1), 255–263.
17 Wei Song, *et al.*, Dynamic self-organization of microwell-aggregated cellular mixtures, *Soft Matter*, 2016, **12**(26), 5739–5746.
18 A. Haeger, *et al.*, Cell jamming: collective invasion of mesenchymal tumor cells imposed by tissue confinement, *Biochim. Biophys. Acta, Gen. Subj.*, 2014, **1840**(8), 2386–2395.
19 K. Wolf and P. Friedl, Extracellular matrix determinants of proteolytic and non-proteolytic cell migration, *Trends Cell Mol. Biol.*, 2011, **21**(12), 736–744.
20 S. B. Anderson, *et al.*, The performance of human mesenchymal stem cells encapsulated in cell-degradable polymer-peptide hydrogels, *Biomaterials*, 2011, **32**(14), 3564–3574.
21 D. R. Griffin, W. M. Weaver, P. O. Scumpia, D. Di Carlo and T. Segura, Accelerated wound healing by injectable microporous gel scaffolds assembled from annealed building blocks, *Nat. Mater.*, 2015, **14**(7), 737–744.
22 O. Chaudhuri, L. Gu, D. Klumpers, M. Darnell, S. A. Bencherif, J. C. Weaver and D. J. Mooney, Hydrogels with tunable stress relaxation regulate stem cell fate and activity, *Nat. Mater.*, 2016, **15**(3), 326–334.
23 V. Estrada, N. Brazda, C. Schmitz, S. Heller, H. Blazyca, R. Martini and H. W. Müller, Long-lasting significant functional improvement in chronic severe spinal cord injury following scar resection and polyethylene glycol implantation, *Neurobiol. Dis.*, 2014, **67**, 165–179.
24 S. Allazetta, L. Kolb, S. Zerbib, J. A. Bardy and M. P. Lutolf, Cell-Instructive Microgels with Tailor-Made Physicochemical Properties, *Small*, 2015, **11**(42), 5647–5656.
25 C. D. Morley, *et al.*, Quantitative characterization of 3D bioprinted structural elements under cell generated forces, *Nat. Commun.*, 2019, **10**(1), 1–9.
26 T. Bhattacharjee, *et al.*, Liquid-like solids support cells in 3D, *ACS Biomater. Sci. Eng.*, 2016, **2**(10), 1787–1795.
27 T. Bhattacharjee and S. D. Sujit, Bacterial hopping and trapping in porous media, *Nat. Commun.*, 2019, **10**(1), 1–9.
28 T. Bhattacharjee and S. D. Sujit, Confinement and activity regulate bacterial motion in porous media, *Soft Matter*, 2019, **15**(48), 9920–9930.
29 T. Bhattacharjee and E. A. Thomas, 3D T cell motility in jammed microgels, *J. Phys. D: Appl. Phys.*, 2018, **52**(2), 024006.
30 T. Bhattacharjee, *et al.*, Writing in the granular gel medium, *Sci. Adv.*, 2015, **1**(8), e1500655.
31 C. S. O'Bryan, *et al.*, Self-assembled micro-organogels for 3D printing silicone structures, *Sci. Adv.*, 2017, **3**(5), e1602800.
32 C. S. O'Bryan, *et al.*, Three-dimensional printing with sacrificial materials for soft matter manufacturing, *MRS Bull.*, 2017, **42**(8), 571–577.
33 T. Bhattacharjee, *et al.*, Polyelectrolyte scaling laws for microgel yielding near jamming, *Soft Matter*, 2018, **14**(9), 1559–1570.
34 A. Bhattacharyya, C. O'Bryan, Y. Ni, C. D. Morley, C. R. Taylor and T. E. Angelini, Hydrogel compression and polymer osmotic pressure, *Biotribology*, 2020, 100125.
35 K. D. Schulze, S. M. Hart, S. L. Marshall, C. S. O'Bryan, J. M. Urueña, A. A. Pitenis and T. E. Angelini, Polymer osmotic pressure in hydrogel contact mechanics, *Biotribology*, 2017, **11**, 3–7.
36 X. Duportet, *et al.*, A platform for rapid prototyping of synthetic gene networks in mammalian cells, *Nucleic Acids Res.*, 2014, **42**(21), 13440–13451.
37 J. S. Ballez, *et al.*, Plant protein hydrolysates support CHO-320 cells proliferation and recombinant IFN-γ production in suspension and inside microcarriers in protein-free media, *Cytotechnology*, 2004, **44**(3), 103–114.
38 K.-i. Nishijima, *et al.*, The effects of cell adhesion on the growth and protein productivity of animal cells, *Cytotechnology*, 2000, **33**(1–3), 147–155.
39 M. F. Krummel, R. S. Friedman and J. Jacobelli, Modes and mechanisms of T cell motility: roles for confinement and Myosin-IIA, *Curr. Opin. Cell Biol.*, 2014, **30**, 9–16.

40 M. D. Rintoul and T. Salvatore, Precise determination of the critical threshold and exponents in a three-dimensional continuum percolation model, *J. Phys. A: Math. Gen.*, 1997, **30**(16), L585.
41 W. Xu, S. Xianglong and J. Yang, Continuum percolation of congruent overlapping spherocylinders, *Phys. Rev. E*, 2016, **94**(3), 032122.
42 E. J. Garboczi, *et al.*, Geometrical percolation threshold of overlapping ellipsoids, *Phys. Rev. E: Stat. Phys., Plasmas, Fluids, Relat. Interdiscip. Top.*, 1995, **52**(1), 819.
43 Y.-B. Yi and A. M. Sastry, Analytical approximation of the percolation threshold for overlapping ellipsoids of revolution, *Proc. R. Soc. London, Ser. A*, 2004, **460**(2048), 2353–2380.
44 S. E. Leggett, *et al.*, Motility-limited aggregation of mammary epithelial cells into fractal-like clusters, *Proc. Natl. Acad. Sci. U. S. A.*, 2019, **116**(35), 17298–17306.
45 A. Lee, *et al.*, 3D bioprinting of collagen to rebuild components of the human heart, *Science*, 2019, **365**(6452), 482–487.
46 S. R. Moxon, *et al.*, Suspended manufacture of biological structures, *Adv. Mater.*, 2017, **29**(13), 1605594.
47 C. B. Highley, *et al.*, Jammed microgel inks for 3D printing applications, *Adv. Sci.*, 2019, **6**(1), 1801076.
48 K. H. Song, *et al.*, Complex 3D-Printed Microchannels within Cell-Degradable Hydrogels, *Adv. Funct. Mater.*, 2018, **28**(31), 1801331.
49 O. Jeon, *et al.*, Individual cell-only bioink and photocurable supporting medium for 3D printing and generation of engineered tissues with complex geometries, *Mater. Horiz.*, 2019, **6**(8), 1625–1631.
50 O. Jeon, *et al.*, Cryopreserved cell-laden alginate microgel bioink for 3D bioprinting of living tissues, *Mater. Today Chem.*, 2019, **12**, 61–70.
51 S. Xin, *et al.*, Clickable PEG hydrogel microspheres as building blocks for 3D bioprinting, *Biomater. Sci.*, 2019, **7**(3), 1179–1187.
52 A. M. Douglas, A. A. Fragkopoulos, M. K. Gaines, L. A. Lyon, A. Fernandez-Nieves and T. H. Barker, Dynamic assembly of ultrasoft colloidal networks enables cell invasion within restrictive fibrillar polymers, *Proc. Natl. Acad. Sci. U. S. A.*, 2017, **114**(5), 885–890.

Electronic Supplementary Material (ESI) for Soft Matter.

Supplementary Information

3D self-assembly of cells in packed microgel media

Cameron D. Morley, Jesse Tordoff, Christopher S. O'Bryan, Ron Weiss, Thomas E. Angelini

Supplemental Text

Cell body fluctuations. To investigate how fluctuations in cell shape may influence aggregation, we measure the extent of the longest axis of every isolated object detected in time-lapse confocal fluorescence z-stacks at every point in time, $L(t)$. Stacks are processed as decribed in section 2.5 in the manuscript body. The 'PrincipalAxisLength' measurement within the regionprops3 function in MATLAB is used to determine $L(t)$, returning the length of the longest axis of every object. Particle tracking is perfomed to link the same objects together over time. Since cells don't migrate through the gel, tracking is fairly stratight-forward. When objects merge, the earlier tracks are terminated and a new track is started for the new object. To statistically analyze fluctuations of all individual objects over time, we compute the mean-square-fluctuations of each individual $L(t)$, given by $\Delta L^2(\tau) = \left\langle \left(L(t+\tau) - L(t) \right)^2 \right\rangle_t$, where the angle brackets indicate an average over time, t. To test whether $\Delta L^2(\tau)$ exhibits any dependence on the size of the objects, we analyze scatter plots of $\Delta L^2(\tau)$ versus $\langle L \rangle_t$ at each lag time, τ, where $\langle L \rangle_t$ is the average of $L(t)$ over time for each individual object. At any given lag time, τ, we see no clear length-scale dependence, yet the overall point cloud increases to higher values of ΔL^2 with increasing τ (Fig. S4a). To decide how to analyze the ensemble, we create histograms of ΔL^2 for each lag time, τ. We find these ΔL^2 distributions to be highly asymmetric when binned linearly, but more symmetric when binned logarithmically. We find that the distributions are not well described by log-normal statistics, but the median value of ΔL^2 corresponds well to the peaks in the histograms at each lag time, τ (Fig. S4b). Thus, at each lag time we use the median value of ΔL^2 as the representative

square-fluctuation averaged over the population of *n* objects, $\left\langle \Delta L^2(\tau) \right\rangle_n$. A plot of $\left\langle \Delta L^2(\tau) \right\rangle_n$ versus τ reveals that below τ = 2 h, fluctuations grow like $\tau^{1/2}$, and for t between 2 h and 6 h, fluctuations grow like $\tau^{0.9}$ (Fig S4c). From the square-root of $\left\langle \Delta L^2(\tau) \right\rangle_n$, it can be seen that the representative fluctuation in the extent of any of the objects is about 11 μm over the course of about 6 h. The consequences of this result are discussed in the text.

Supplemental Figures

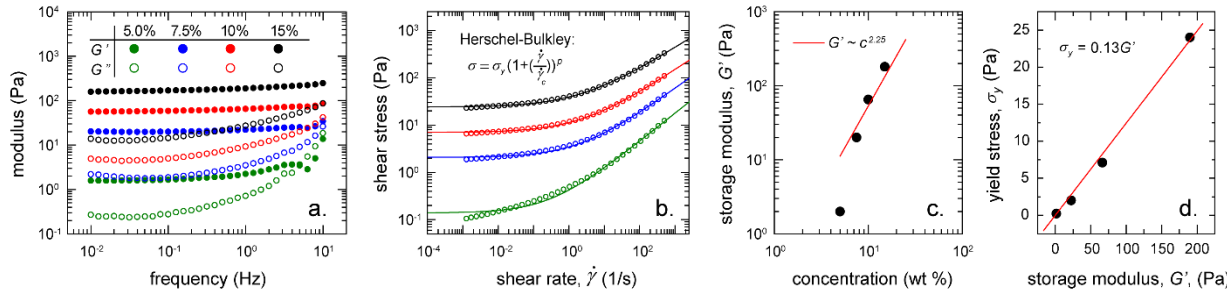

Fig. S1. We conduct rheological characterization of the packed microgel culture media used in our cell aggregation studies. (a) Frequency sweeps at 1% strain amplitude show that the elastic modulus, *G'*, and viscous modulus, *G''* increase with increasing microgel concentration. For most concentrations, *G'* >> *G''* across three decades of frequencies. For the sample at lowest microgel concentration, *G''* begins to dominate *G'* at high frequencies. (b) Unidirectional shear tests exhibit plateaus in shear stress at low shear rates and sub-linear rises in shear stress at high shear rates, as expected of these packed microgel systems. These data are fit to the Herschel-Bulkley model to determine the yield stress. (c) plotting *G*' versus polymer concentration for the packed microgels, we see a sharp increase near the jamming concentration of approximately 4% polymer. At concentrations in the 10-15% range, *G*' raises in a manner consistent with $c^{9/4}$. Such a scaling would suggest that within this concentration range, the pore space between microgels is squeezed out and the jammed system behaves like a continuous gel. (d) Plotting yield stress versus *G'* evaluated at 1 Hz shows the same linear relationship previouisly established in comparable microgel systems.

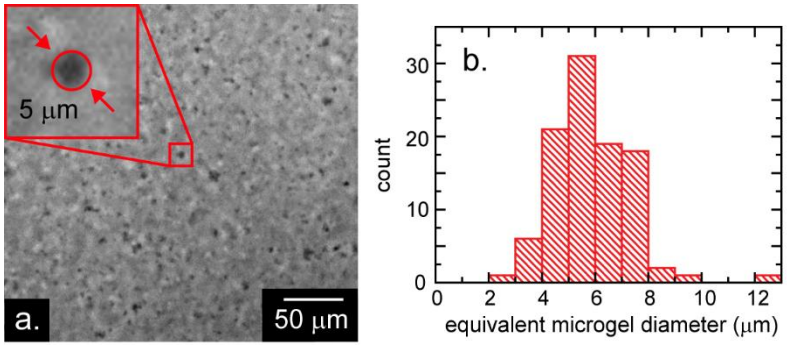

Fig. S2. (a) We examine a diluted sample of microgels under phase contrast microscopy. (b) To determine microgel size, we outline particles from these images and measure their areas using imageJ. Equating these areas to those of equivalent circles, we calculate the equivalent microgel diameter and generate a histogram to find that the average microgel particle is 5 – 6 μm in diameter.

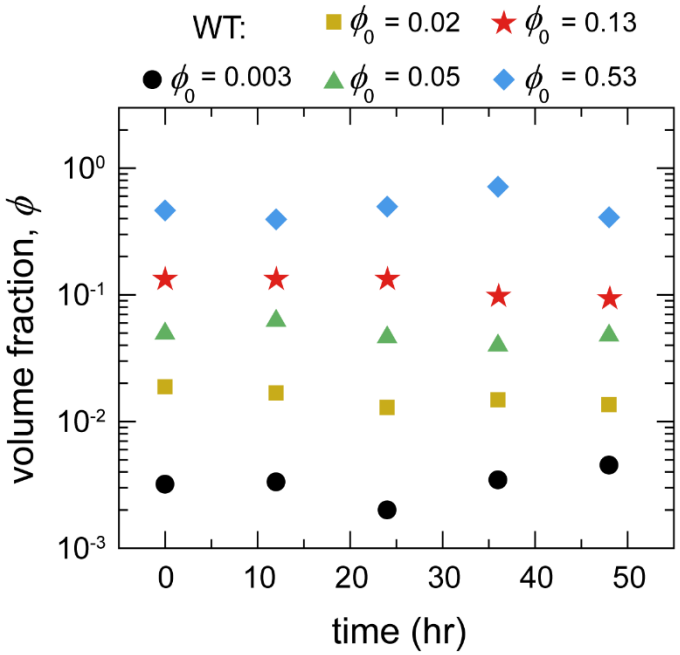

Fig. S3. The average sample volume fraction exhaibits small fluctuations over time relative to the large differences set by the seeding volume fraction. This behavior is consistent with our observing almost no proliferation over the 48 h experiments.

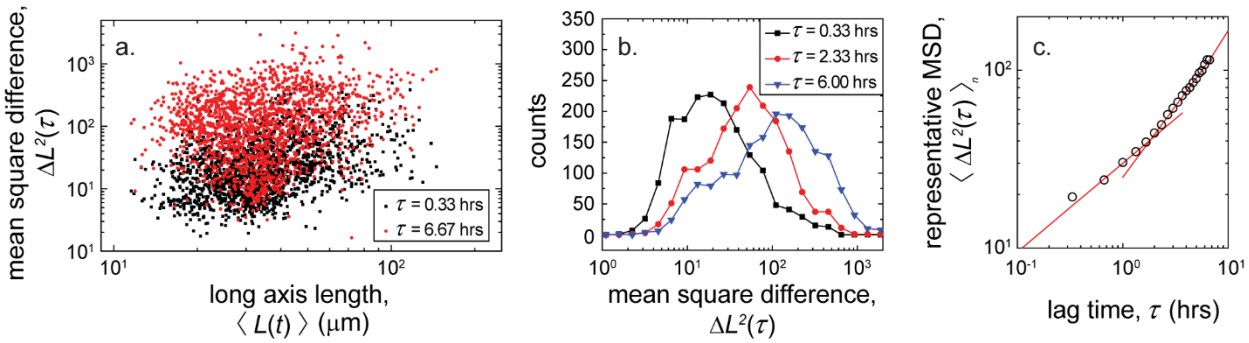

Fig. S4. (a) At any given lag time, τ, we see no clear length-scale dependence of ΔL^2 on L, yet the overall point cloud increases to higher values of ΔL^2 with increasing τ. (b) To choose a represntative ΔL^2 for each t, we perform histogram analysis, finding that the distributions are fairly symmetric when ΔL^2 is sampled logarithmically. We find that the median of ΔL^2 lays close to the peaks in these histograms. (c) Plotting the ensemble-averaged median value of ΔL^2 versus τ, we see that fluctuations in extent of all detected objects exhibit sub-diffusive dynamics. ΔL^2 grows like $\tau^{1/2}$ and short times and like $\tau^{0.9}$ at long times (red lines).

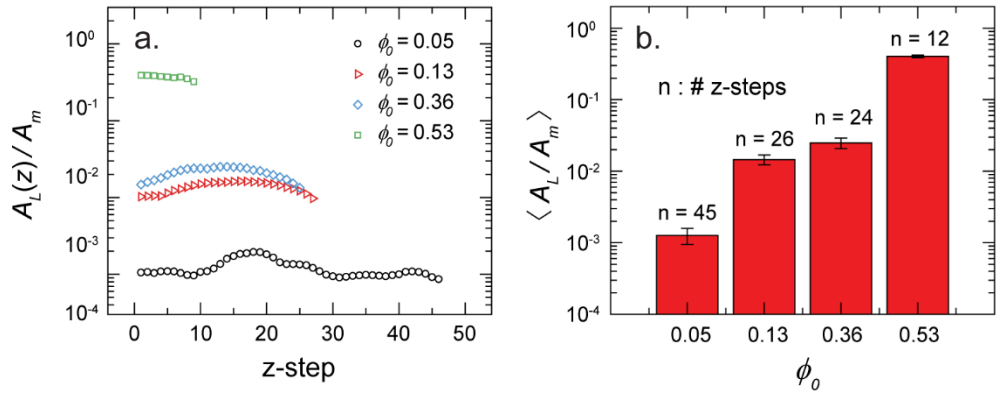

Fig. S5. To test the quality of our imaging as a function of depth into the samples, we examine how A_L / A_m depends on the location along the optical axis of each optical section (z-step). (a) We find that A_L / A_m exhibits no dominating trend as we step into the samples compared to diffferences between samples prepared at different cell volume fractions. We note that we intentionally decrease overall stack thickness with increasing cell density because of light attenuation. (b) Computing the mean and standard deviation of each set of A_L / A_m from (a), we see the relative variations about about the mean decreasing slightly with increasing volume fraction (errorbars denote ± one standard deviation).